SOURCE SIGNATURE ESTIMATION BASED ON RECORDINGS IN DEEP-TOWED STREAMERS BELOW THE SOURCE

Kristian Svarva Helgebostad[1], Martin Landrø[2], Vetle Vinje[3], Carl-Inge Nilsen[3]

[1] Formerly M.Sc student at Norwegian University of Science and Technology/CGG, presently

with PGS. E-mail: kristian.svarva.helgebostad@pgs.com

[2] Norwegian University of Science and Technology, Department of Geoscience and Petroleum.

E-mail: martin.landro@ntnu.no

[3]CGG. E-mail: vetle.vinje@cgg.com; carl-inge.nilsen@cgg.com

ABSTRACT

Recent developments in marine seismic acquisition includes deploying a source vessel above a towed-streamer spread. Such acquisition configurations provide increased knowledge about the emitted source signature, because the direct wave is recorded below the source. We present an inversion algorithm for estimating source signatures based on the recordings of the direct wave, assuming that it is recorded below the source. The forward modeling of the algorithm is based upon a physical modeling of the air bubble created by each air gun in the source array. A damped Gauss-Newton approach is used as a search algorithm to minimize the difference between the recorded and modeled direct wave. Typical inversion parameters are empirical damping factors for the bubble oscillations and firing time delays for each air gun. Variations in streamer depth are taken into account and a constant sea surface reflection coefficient is also estimated as a by-product of the inversion. For shallow water data sets, we propose to extend the forward modeling of the inversion scheme to include reflections from the water bottom. The algorithm is tested on synthetic and field data examples. For the field data example, the estimated source signatures give sensible results when used in a designature flow.

INTRODUCTION

Source signature estimation is an important problem in reflection seismology, because knowledge about the source signature is key to numerous steps in processing and analysis of the seismic data. Helgesen and Landrø (1993) and Landrø et al. (1993) show some examples where the result depends on the quality of the estimated source signature. Because of the challenges and high cost in measuring the source signature directly in marine seismic acquisition, researchers

have proposed various strategies to estimate source signatures. For example, source signatures can be estimated using statistical methods (Robinson and Treitel, 1980; Oldenburg et. al., 1981), wave-theoretical methods of source signature extraction (Weglein and Secrest, 1990; Osen et. al., 1998), methods based on seismic interferometry (Behura and Snieder, 2013) or methods based on inversion, assuming that the direct wave-field is recorded at different locations close to the source (Ziolkowski et. al., 1982; Landrø and Sollie, 1992; Amundsen, 1993). The method described by Ziolkowski et al. (1982) is a common approach today, where the source signature is estimated based on recordings in near-field hydrophones. The basic idea of this method is to remove the effect of the neighbouring sources and their ghosts on each near-field measurement to obtain effective point sources. The effective point sources can then be superposed to calculate the far-field source signature from the full source array. An alternative approach was proposed by Landrø and Sollie (1992), where they use recordings on a mini-streamer below the source to estimate source signatures. The algorithm was later tested on field data examples by Landrø et al. (1994), while Laws et al. (1998) compared the two methods for several configurations.

Recent advances in marine seismic acquisition includes deploying a source vessel above a towed streamer-spread (Vinje et al. 2017). Such acquisition configurations open the possibility for estimating source signatures in a similar fashion as Landrø and Sollie (1992), because the direct wave is recorded below the source. We present a modified version of the algorithm proposed by Landrø and Sollie (1992) to estimate source signatures from acquisition configurations where the direct wave is recorded below the source. The method estimates notional source signatures (effective point sources) using an inversion algorithm so that directional far-field signatures can be estimated on a shot-by-shot basis.

THEORY

Modeling

Rayleigh (1917) studied the collapse of a spherical cavity in an incompressible fluid and showed that the collapse time for such a cavity is a function of the initial bubble radius, the density of the fluid and the hydrostatic pressure surrounding the cavity. Later, Johnson (1994) presented an alternative equation to describe the bubble motion in an infinite volume of water. We use a modified Johnson-equation to describe the bubbles from each air gun in the source array,

$$\ddot{R} = \frac{P - p_\infty}{R\rho} - \frac{3}{2R}\dot{R}^2 + \gamma\frac{1}{\rho c}\dot{p} + \alpha\frac{\dot{R}}{R} + \beta(t)\frac{\dot{R}^2}{R} \tag{1}$$

where R is the bubble radius as a function of time, dot denotes the time derivative of the function, P is the pressure inside the bubble, p_∞ is the hydrostatic pressure at the depth of the bubble, ρ and c are the density and velocity of the water, respectively and γ is a fixed constant introduced by Johnson (1994) to fit measurements. α and $\beta(t)$ are empirical factors that control the damping of the bubble and the bubble time period, inspired by Landrø and Sollie (1992). To take into account that the bubble time period between each oscillation can vary due to the interaction between the bubbles, $\beta(t)$ is a time-variant factor, given by $\beta(t) = \beta_0 + \beta_1 t$. After solving Equation 1 for $R(t)$, the pressure at the bubble wall can be described by,

$$P(R) = P_0 \left(\frac{R_0}{R}\right)^{3\lambda} \tag{2}$$

where P_0 and R_0 are the initial pressure and radius of the air bubble, R is the radius of the cavity

as a function of time and λ is a gas constant. λ can for example be set to $\lambda = 1$, assuming

isothermal bubble expansion, or $\lambda = 1.4$ for adiabatic bubble expansion. We have used $\lambda = $

1.13, similar to the value used by Ziolkowski (1970).

The pressure field at a far-field point from the bubble center, created by a single

oscillating air bubble, was derived by Gilmore (1952) and can be written in the form,

$$p - p_\infty = \rho_\infty \frac{R}{r} (H + \frac{\dot{R}^2}{R}) \tag{3}$$

where p is the acoustic pressure, r is the distance between the bubble center and the far-

field point and H is the enthalpy at the bubble wall. Higher order terms of $\frac{1}{r}$ are neglected, and

the effect of the free surface is not taken into account. For the enthalpy at the bubble wall in

Equation 3, we use the approximation,

$$H \approx \frac{P - p_\infty}{\rho} \tag{4}$$

A more precise expression for the enthalpy is to use the Tait equation, as described by

Landrø (1992). For an array consisting of several air guns, the total pressure at a certain far-field

position is given as a simple superposition of the pressure output from each individual source.

The pressure field from each source is modified due to interaction effects between the guns. In

the presented algorithm, the interaction effects are taken into account by introducing the

empirical factors α and $\beta(t)$. Then, the acoustic pressure at a far-field point is given as,

$$d(t) = \sum_{i=1}^{N} \left[\frac{1}{r_i} s_i \left(t - \tau_i - \frac{r_i}{c} \right) + \eta \frac{1}{r_i^g} s_i \left(t - \tau_i - \frac{r_i^g}{c} \right) \right] \qquad (5)$$

where N is the number of air guns, s_i and τ_i are the notional source signature and firing

time delay for air gun i, c is the water velocity, η the sea surface reflection coefficient and r_i and

r_i^g the distance and ghost distance between air gun i and the far-field point, respectively. Note

that s_i is the notional source signature of air gun i (where interaction effects are included). The

modeled pressure at each of the hydrophones can then be calculated using Equation 5.

Extending the forward modeling to include the water bottom reflection

When data are acquired in relatively deep water, the water bottom reflection does not

interfer with the direct wave to a significant degree. However, in shallower water, the water

bottom reflection can cause problems for methods that try to extract information from the direct

wave. Hopperstad and Laws (2006) suggest to include the water bottom reflection in the forward

modeling when notional source signatures are estimated from near-field hydrophone

measurements in very shallow water. Similarly, we can extend the forward modeling in the

presented algorithm to model the water bottom reflection by modifying Equation 5,

$$d(t) = \sum_{i=1}^{N} \left[\frac{1}{r_i} s_i \left(t - \tau_i - \frac{r_i}{c} \right) + \eta \frac{1}{r_i^g} s_i \left(t - \tau_i - \frac{r_i^g}{c} \right) + \cdots \right.$$

$$\kappa \frac{1}{r_i^{wb}} s_i \left(t - \tau_i - \frac{r_i^{wb}}{c} \right) + \kappa \eta \frac{1}{r_i^{wb_{sg}}} s_i \left(t - \tau_i - \frac{r_i^{wb_{sg}}}{c} \right) + \cdots \qquad (6)$$

$$\left. \kappa \eta \frac{1}{r_i^{wb_{rg}}} s_i \left(t - \tau_i - \frac{r_i^{wb_{rg}}}{c} \right) + \kappa \eta^2 \frac{1}{r_i^{wb_{srg}}} s_i \left(t - \tau_i - \frac{r_i^{wb_{srg}}}{c} \right) \right]$$

where κ is the reflection coefficient at the water bottom and r_i^{wb}, r_i^{wbsg}, r_i^{wbrg}

and r_i^{wbsrg} are the travel distance for the primary reflection, source ghost, receiver ghost

and source receiver ghost from the water bottom, respectively. For simplicity, we

assume that the reflection coefficient is independent of income angle in the modeling of

the water bottom reflection.

Inversion scheme

The goal of the inverse problem is to recover a model that explains the observed data. In

our algorithm, we aim to find a set of notional source signatures that minimizes the difference

between the modeled direct wave and the observed data. This can be formulated by minimizing a

data misfit function, φ_d,

$$\varphi_d = \sum_i^{N_r} \sum_j^{N_t} \left(d(\vec{x_i}, t_j) - d^{obs}(\vec{x_i}, t_j) \right)^2 \tag{6}$$

where $d(\vec{x_i}, t_j)$ and $d^{obs}(\vec{x_i}, t_j)$ are the modeled and measured pressure at time t_j and

receiver position $\vec{x_i}$, respectively, N_r is the number of receivers and N_t is the number of time

samples.

To avoid numerical instabilities related to the large magnitude differences between the model parameters, the following scaling procedure is applied (similar to e.g Helgesen and Landrø (1993)),

$$\tilde{H}_{ij} = \frac{H_{ij}}{\sqrt{H_{ii}H_{jj}}}$$

(7)

$$\tilde{g}_i = \frac{g_i}{\sqrt{H_{ii}}}$$

where $H \approx J^T J$ is the approximate Hessian matrix and J is the Jacobian matrix. The Jacobian matrix is equal to the derivative of the modeled signal with respect to the model parameters, which means that $J_{ij} = \frac{\delta d_i}{\delta m_j}$ where i runs over the data space and j over the model space. The Jacobian matrix is calculated with a finite difference approximation. The gradient, g, is given by $g = J^T \Delta d$, where Δd is the data residual vector, $\Delta d = d - d^{obs}$.

We use a damped Gauss-Newton algorithm for the optimization. The scaled model parameter updates are therefore given as

$$\Delta \tilde{m} = (\tilde{H} + \psi I)^{-1} \tilde{g}$$

(8)

where ψ is the Levenberg-Marquardt damping parameter (Marquardt, 1963) and I is the identity matrix. ψ is unchanged for the first iteration of the inversion loop and for subsequent iterations scaled by the relative error between the real and modeled data.

The unknown parameters that we invert for are α and $\beta(t)$ and a frequency and angle-independent sea surface reflection coefficient. Additionally, streamer depths and firing time delays are not accurately known in practice, so they are also included as unknown model parameters. However, it is not practical to include the depth of each hydrophone in the inversion scheme. Therefore, we describe the shape of each streamer as a limited Fourier series with a gradient term,

$$z(x) = z_r + cx + \sum_{n=1}^{K} \left[a_n \cos\left(\frac{2\pi n x}{L}\right) + b_n \sin\left(\frac{2\pi n x}{L}\right) \right] \tag{9}$$

where z_r is the average depth of the receivers along the streamer, L is the horizontal distance between the start and end of the part of the streamer that is included in the inversion, a_n and b_n are Fourier coefficients, c is a gradient term and K is the number of Fourier coefficients. This function will express the receiver depths along each streamer reasonably well, without using too many unknown model parameters to describe them.

When the inversion is carried out for the full bandwidth of the data, the model parameters that control the primary pulse of the direct wave will dominate (e.g. firing time delays and streamer depths). Therefore, the inversion is first carried out for the low-frequency part of the data, where only α and $\beta(t)$ and the sea surface reflection coefficient are inverted for. Then, the estimated parameters from the low-frequency part of the data are used as initial parameters when the inversion is carried out for the full bandwidth of the data, where also the streamer shape and firing time delays are inverted for. This approach has similarities to what is done in full waveform inversion, where Bunks et al. (1995) propose multiscale seismic waveform inversion because the objective function has less local minima for long wavelengths.

RESULTS

Synthetic data examples

For the inversion experiments with synthetic data, we simulate data in two types of environments; deep and shallow water. For the deep water data set, we assume that subsurface scattering is negligible, i.e. we do not include the water bottom reflection and its ghost in the forward modeling of the inversion scheme. However, for the shallow water data set, we include the water bottom reflection and its ghost in the forward modeling to stabilize the inversion, as the reflections will now mingle with the direct wave to a larger degree.

We model the synthetic data sets from a source array with a configuration as presented in Table 1. The source array consists of two sub-arrays with 5 air guns each. The sub-arrays are 6 m apart, and the distance between each air-gun in the sub-arrays is 3 m. The gun depth for all air guns is 7.5 m and the firing pressure (P_0) is 137 bar. The data are filtered with a Seal LinP3 OUT 3-6 200-370 instrument filter.

We only model the pressure wave-field at receivers that are relatively close to the source, where the amplitude difference between the direct wave and reflections is large. The acquisition configuration, with the receivers from the three streamers that are included in the modeling, is shown in Figure 1. In Figure 2, we show the shape of the streamers for the reference model (solid blue) and for the initial model for the inversion (dashed red).

The sea surface reflection coefficient is included as an unknown model parameter in the inversion. The reflection coefficient for the reference model is set to $\eta = -0.95$, while it is set to

$\eta = -1$ for the initial model for the inversion. The remaining model parameters for the reference

model and for the initial model are shown in Figure 3.

Deep water data set

For the deep water case, reflections from a flat seabed at 300 m depth below the sea

surface, are included in the modeling of the synthetic data. The reflection coefficient at the

seabed interface is for simplicity independent of income angle and set to 0.3.

In Figure 4a, we show the modeled data for the reference model, divided into three boxes,

corresponding to the three streamers, while we show the residual signal after the inversion in

Figure 4b. We observe that the reflections from the subsurface remain in the residual signal, as

expected, since they are not included in the forward modeling in the inversion scheme. The

relative RMS error between the modeled data with the reference model and the initial model is

4.95 %, while it is reduced to 0.53 % after the inversion. The estimated sea surface reflection

coefficient after the inversion is $\eta = -0.9479$ after the inversion, in good agreement with the

true value of $\eta = -0.95$. The estimated streamer shapes (dashed red) are compared to the true

streamer shapes (solid blue) in Figure 5. The remaining model parameters are shown in Figure 6.

α and β_0 are well estimated, while there are larger deviations between the estimated and true

values for β_1. β_1 was better estimated in inversion experiments with no reflections in the data,

indicating that the deviations between the true and estimated β_1-values are caused by the water

bottom reflection in this data set. β_1 control how the bubble time varies from the first to the

second and third bubble collapse, and is therefore less constrained by the first bubble pulse than

α and β_0. Hence, β_1 is expected to be most disturbed by reflections from the subsurface. Both

the estimated firing time delays and streamer shapes deviate from the true model to some degree;

the average error of the estimated firing time delays and receiver depths was 0.05 ms and 0.2 m, respectively. We notice that the general trend is that the estimated receiver depths are too shallow and that the estimated firing time of the air guns is too late. This is reasonable, as these errors will counteract with regards to the travel time of the direct wave, relative to a time zero.

The calculated notional source signatures from the estimated model parameters are shown in Figure 7. As discussed by Landrø et al. (1991), the near-field to far-field method has a tendency to introduce ripples in the notional source signatures that are not observed in the far-field measurements. We notice that the amount of such ripples is low in the notional source signatures in Figure 7.

Shallow water data set

For the shallow water case, the water depth is 69 m and the angle-independent reflection coefficient at the seabed interface is 0.3. As the water bottom reflection and its ghost are now included in the forward modeling of the inversion scheme, these parameters will also be estimated. We have used initial values of 70 m and 0.35 for the water depth and reflection coefficient at the seabed interface.

In Figure 8a, we show the modeled data for the reference model, divided into three boxes, corresponding to the three streamers, while we show the residual signal after the inversion in Figure 8b. Contrary to the deep water case, the reflections do now not appear in the residual signal, as we have included the reflections in the forward modeling in the inversion scheme.

The relative RMS error between the modeled data with the reference model and the initial model is 5.57 %, while it is reduced to 4.21×10^{-7} % after the inversion. The sea surface

reflection coefficient, water depth and reflection coefficient at the seabed are estimated very well - the true values are almost recovered exactly. The estimated streamer shapes (Figure 9) and remaining model parameters (Figure 10) are also estimated very accurately. We notice that β_1 is estimated more accurately than in the deep water case, now that the reflections are included in the forward modeling of the inversion scheme. The notional source signatures calculated from the estimated model parameters are shown in Figure 11.

Real data example

The algorithm is tested on a shot-gather acquired in deep water offshore Gabon with CGGs source-over-spread acquisition design (Vinje et al. 2017). As the data are acquired in deep water, we assume that subsurface scattering is negligible, which means that we only model the direct wave in the forward modeling of the inversion scheme. In Figure 12, we show the location for the source array and for the receivers that were included in the inversion. The direct wave recorded at the receivers directly below the source was clipped due to overloading of the hydrophones. Therefore, these receivers were not included in the inversion. This did not affect the stability of the inversion as subsurface scattering was negligible also for the receivers close to the source that were not overloaded. However, for data sets in shallower waters, the receivers that are closest to the source should be included to stabilize the inversion.

For the clustered air guns in the source array, we assume that these can be modeled as one single air gun with an air gun volume equal to the volume of the air guns in the cluster. This is done for simplicity, and more accurate modeling of the clusters can improve the quality of the forward modeling of the algorithm.

The relative RMS error between the real data and the modeled direct wave from the initial model is 31.9 %, while the residual RMS error after the inversion is 21.9 %. We note that the residual RMS error is significantly higher for the field data example than the synthetic deep water example. This is mostly due to inaccurate parameters that are not inverted for; the RMS error will for example be affected by inaccurate lateral streamer positions. The sea surface reflection coefficient is estimated to be $\eta = -0.961$. Based on the estimated model parameters from the inversion (Figure 13), we show the corresponding notional source signatures in Figure 14. Similarly to the estimated notional source signatures in the synthetic data examples, we do not observe ripples in the estimated signatures in Figure 14.

The estimated notional source signatures in Figure 14 are used in a designature flow (as explained in Appendix A) with a shot-gather from an inner cable as input. As an intermediate step, we also show the shot-gather after source deghosting. The source deghosting process will boost low frequencies, making bubble energy more visible. In Figure 15, we show input (left), after source deghosting (middle) and after source deghosting and designature (right). The black arrows highlight boosted bubble energy from the water bottom reflection that appears to be zero-phased after the designature process. In Figure 16, we align the water bottom reflection in the shot-gathers. Bubble energy from the water bottom reflection will also align horizontally, as visible where highlighted by black arrows in the shot-gather after deghosting, whereas deeper reflections will not, because they have higher apparent velocity. We also observe that the receiver ghost of the water bottom reflection does not align horizontally, due to the variable-depth profile of the streamer. In Figure 17, we stack the traces in the shot-gathers with the water bottom reflection aligned after deghosting (left) and after deghosting and designature (middle) and the difference between the two (right). Because the water bottom reflection is aligned, it will

add up constructively by the stacking process, while other events will stack out because they have non-horizontal move-out. Low-frequency bubble energy is visible in the deghosted trace, while it is zero-phased in the designatured trace, indicating that the estimated source signatures represent the far-field signature reasonably well. We also note that the receiver ghost appears as a smeared event, as it stacks out due to the variable-depth streamer profile.

DISCUSSION

Landrø et al. (1991) evaluate the near-field to far-field method and find that the method can introduce ripples in the estimated sources that are not observed in far-field measurements. They conclude that this is most likely due to complex physics in the near-field and inaccuracies in the measured positions of the air guns and near-field hydrophones. Ripples are less likely to be introduced in the estimated source signatures with the methods presented by Landrø and Sollie (1992) and in this paper, mainly due to three reasons:

- The methods estimate source signatures based on recordings further away from the source array, where the physics is less complex than in the near-field.
- The methods are less sensitive to inaccuracies in the measured air gun and hydrophone positions. For example, a 10 cm error in the measured hydrophone position will be less significant if the hydrophone is placed 20 m away from the source than if it is placed 1 m away from the source.
- The estimated notional source signatures are based on a physical modeling of oscillating bubbles.

An obvious challenge of estimating source signatures based on recordings further away from the source array is that subsurface scattering is more significant. The near-field to far-field method is robust, even in shallow waters, because the hydrophones are placed close to each air gun. In the extreme cases where subsurface scattering causes problems for the near-field to far-field method, Hopperstad and Laws (2006) suggest to extend the method to include water bottom reverberations. Similarly, we have presented a simple approach for how the water bottom reflection can be included in the forward modeling of the method presented by Landrø and Sollie (1992) and in this paper. The approach has been tested on a synthetic shallow water data set where the assumption of an angle-independent reflection coefficient holds and where the water bottom is horizontal (i.e. how the travel time for the water bottom reflection varies with offset can be calculated easily). The modeling can be extended to more general cases, even though the intention of including the water bottom reflection in the forward modeling of the inversion is to make the inversion more robust, not to model the water bottom reflection perfectly.

CONCLUSION

We have presented an inversion algorithm for source signature estimation, assuming that the direct wave is recorded by conventional streamers below the source. The method is a modified version of earlier literature and extended to modern source-over-spread acquisition configurations. Based on the recordings of the direct wave-field below the source, we estimate effective source signatures for each air gun in the source array that are extrapolated to far-field signatures. The algorithm is tested on synthetic and field data sets. For the synthetic deep water data set, the estimated empirical damping factors are in good agreement with the values from the reference model, while the estimated parameters controlling changes in bubble time period from

the first to the second and third bubble collapse are less accurate. For the synthetic shallow water data set, the water bottom reflection is included in the forward modeling of the inversion scheme to stabilize the inversion, and the model parameters are very well estimated. In the field data example, the estimated notional source signatures were used to designature reflections in shot-gathers.

ACKNOWLEDGMENTS

APPENDICES

APPENDIX A

The objective of the source designature process is to convert the raw seismic wavelet that is recorded from a reflection into a desired wavelet. We use a simple deconvolutional approach for the designature of the seismic data. If we assume that the estimated source signature is $p(\omega)$, where ω is the angular frequency, there is a filter, $f(\omega)$, that can be applied to $p(\omega)$, so that $p(\omega)$ is shaped into a desired wavelet, $G(\omega)$,

$$f(\omega)p(\omega) = G(\omega) \qquad (A\text{-}1)$$

This means that the filter is given by,

$$f(\omega) = \frac{G(\omega)}{p(\omega)} \tag{A-2}$$

Then, the filter, $f(\omega)$, can be applied to the data to shape the embedded wavelets into the desired wavelet. To avoid instabilities where $p(\omega)$ has notches, the filter is regularized,

$$f(\omega) = \frac{G(\omega)}{p(\omega) + \varepsilon} \tag{A-3}$$

where ε is a regularization parameter which limits the boosting of the frequencies in the notch regions.

REFERENCES

Amundsen, L. 1993, Estimation of source array signatures. Geophysics, **58**, no. 12,1865-1869.

Behura, J., and R. Snieder. 2013, Virtual real source: Source signature estimation using seismic interferometry. Geophysics, **78**, no. 5,Q57-Q58.

Bunks, C., F. M. Saleck, S. Zaleski, and G. Chavent. 1995, Multiscale seismic waveform inversion. Geophysics, **60**, no. 5,1457-1473.

Gilmore, F. R. 1952, The growth or collapse of a spherical bubble in a viscous compressible liquid.

Helgesen, J., and M. Landrø. 1993, Estimation of elastic parameters from AVO effects in Tau-P domain. Geophysical Prospecting, **41**, no. 3,341-366.

Hopperstad, J., and R. Laws. 2006, Source Signature Estimation-Attenuation of the Seafloor Reflection Error in Shallow Water. Paper read at 68th EAGE Conference and Exhibition incorporating SPE EUROPEC 2006.

Johnson, D. T. 1994, Understanding air-gun bubble behavior. Geophysics, **59**, no. 11,1729-1734.

Landrø, M. 1992, Modelling of GI gun signatures. Geophysical Prospecting, **40**, no. 7,721-747.

Landrø, M., J. Langhammer, R. Sollie, L. Amundsen, and E. Berg. 1994, Source signature determination from ministreamer data. Geophysics, **59**, no. 8,1261-1269.

Landrø, M., R. Mittet, and R. Sollie. 1993, Implementing measured source signatures in a coarse-grid, finite-difference modeling scheme. Geophysics, **58**, no. 12,1852-1860.

Landrø, M., and R. Sollie. 1992, Source signature determination by inversion. Geophysics, **57**, no. 12,1633-1640.

Landrø, M., S. Strandenes, and S. Vaage. 1991, Use of near-field measurements to compute far-field marine source signatures-Evaluation of the method. First break, **9**, no. 8,375-385.

Laws, R., M. Landrø, and L. Amundsen. 1998, An experimental comparison of three direct methods of marine source signature estimation. Geophysical prospecting, **46**, no. 4,353-389.

Marquardt, D. W. 1963, An algorithm for least-squares estimation of nonlinear parameters. Journal of the society for Industrial and Applied Mathematics, **11**, no. 2,431-441.

Oldenburg, D. W., S. Levy, and K. P. Whittall, 1981, Wavelet estimation and deconvolution. Geophysics, **46**, no. 11,1528-1542.

Osen, A., B. G. Secrest, L. Amundsen, and A. Reitan, 1998, Wavelet estimation from marine pressure measurements. Geophysics, **63**, no. 6,2108-2119.

Rayleigh, L. 1917, VIII. On the pressure developed in a liquid during the collapse of a spherical cavity. The London, Edinburgh, and Dublin Philosophical Magazine and Journal of Science, **34**, no. 200,94-98.

Robinson, E.A., and S. Treitel, 1980, Geophysical signal analysis. Prentice-Hall Inc.

Vinje, V., J. E. Lie, V. Danielsen, P. E. Dhelie, R. Silliqi, C.-I. Nilsen, E. Hicks, and A. Camerer. 2017, Shooting over the seismic spread. First Break, **35**, no. 6,97-104.

Weglein, A. B., and B. G. Secrest, 1990, Wavelet estimation for a multidimensional acoustic or elastic earth. Geophysics, **55**, no. 7,902-913.

Ziolkowski, A. 1970, A method for calculating the output pressure waveform from an air gun. Geophysical Journal International, **21**, no. 2,137-161.

Ziolkowski, A., G. Parkes, L. Hatton, and T. Haugland. 1982, The signature of an air gun array: Computation from near-field measurements including interactions. Geophysics, **47**, no. 10,1413-1421.

LIST OF FIGURES

LIST OF TABLES

Gun	Depth [m]	Vol. [cu.in.]	α [m/s]	β_0 [ ]	β_1 [s^{-1}]
1	7.5	150	4	-0.6	-1.5
2	7.5	150	5	-0.5	0.5
3	7.5	70	2	-0.3	-0.5
4	7.5	70	4	-0.4	-1.5
5	7.5	58	3	-0.5	-0.5
6	7.5	58	5	-0.3	-0.8
7	7.5	113	5	-0.5	0.5
8	7.5	113	4	-0.4	-1
9	7.5	150	2	-0.2	-1.5
10	7.5	150	3	-0.4	-0.5

1
2
3
4
5
6
7
8
9
10
11
12
13
14
15
16
17
18
19
20
21
22
23
24
25
26
27
28
29
30
31
32
33
34
35
36
37
38
39
40
41
42
43
44
45
46
47
48
49
50
51
52
53
54
55
56
57
58
59
60
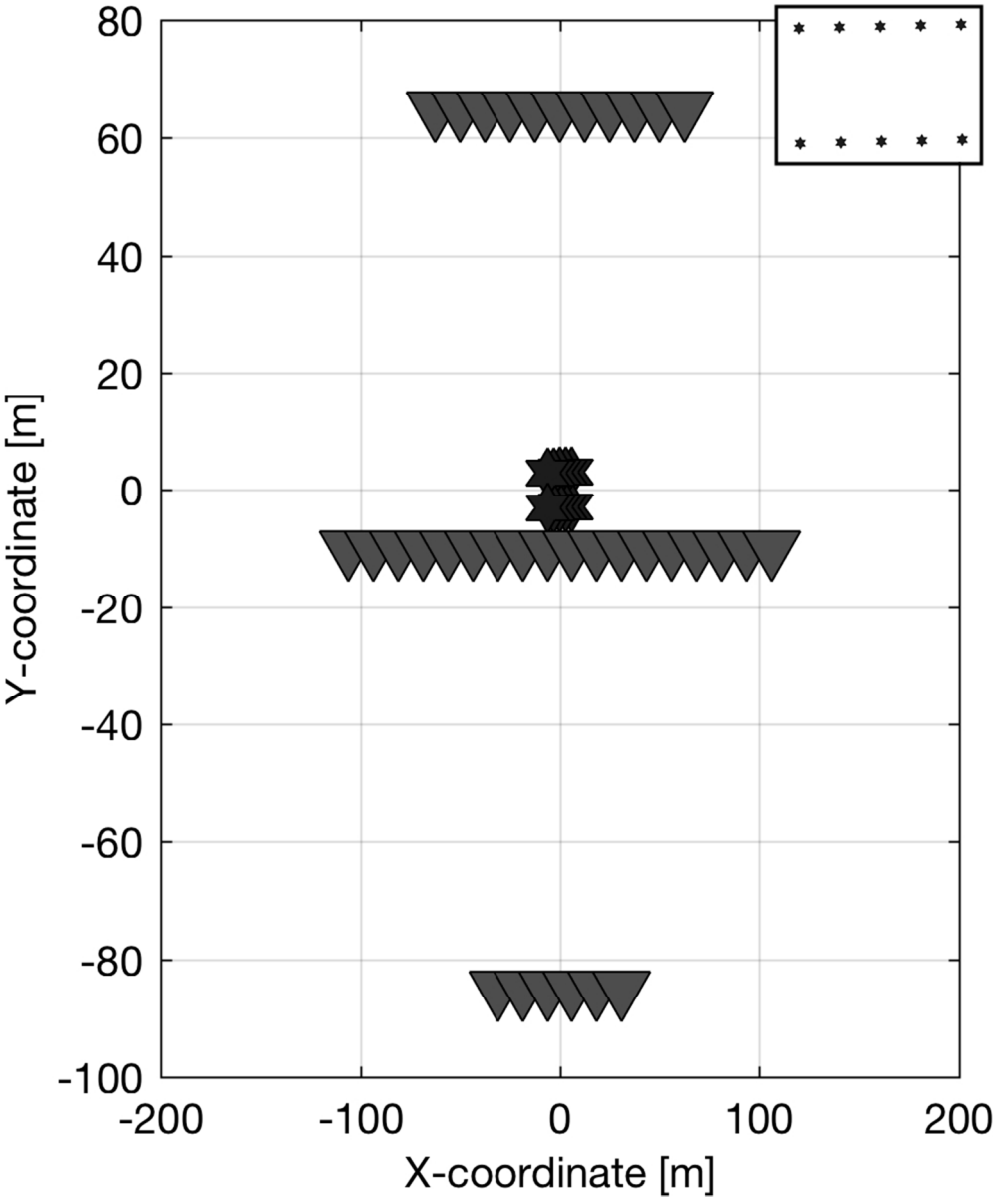
Figure 1: Air gun (stars) and receiver (triangles) locations for the synthetic data examples. Zoom-in of source is displayed in upper right corner.‼ ╂

84x101mm (300 x 300 DPI)
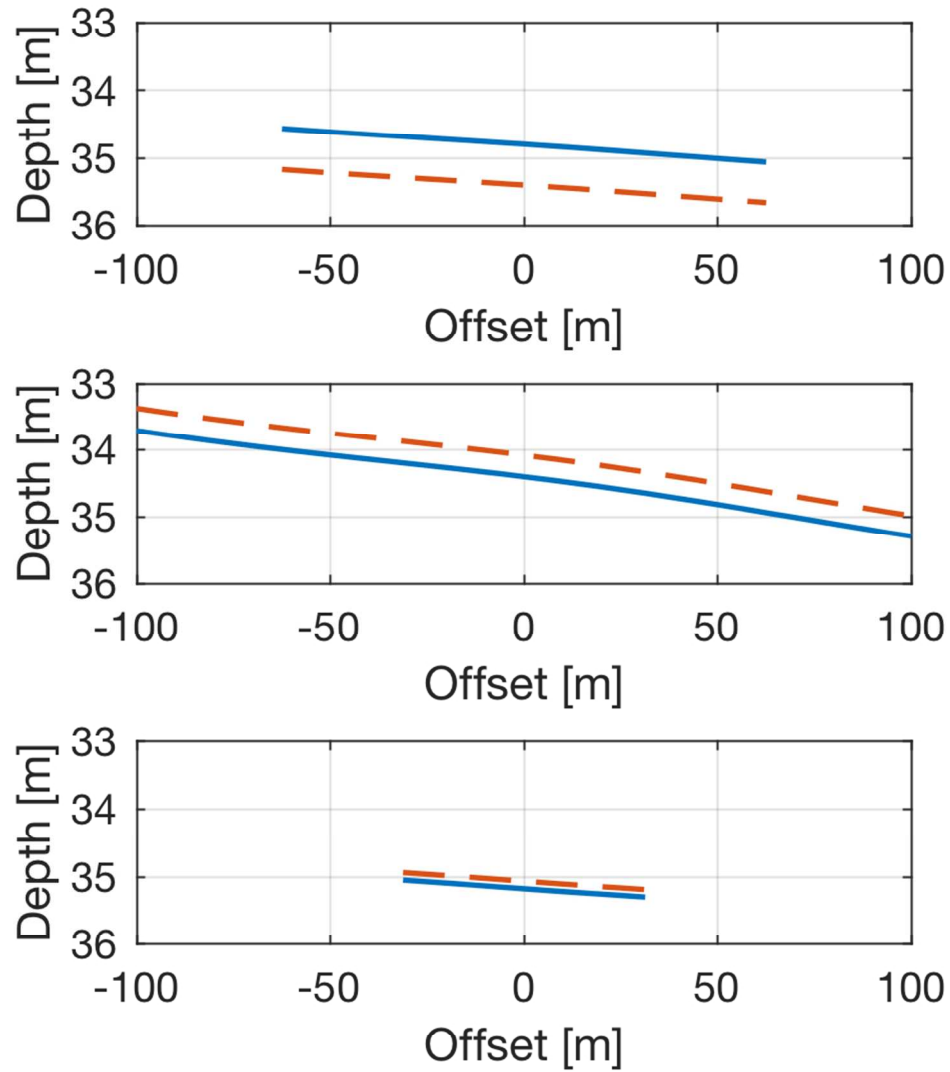
Figure 2: Real (solid blue) and initial (dashed red) model parameters for synthetic inversion experiments.
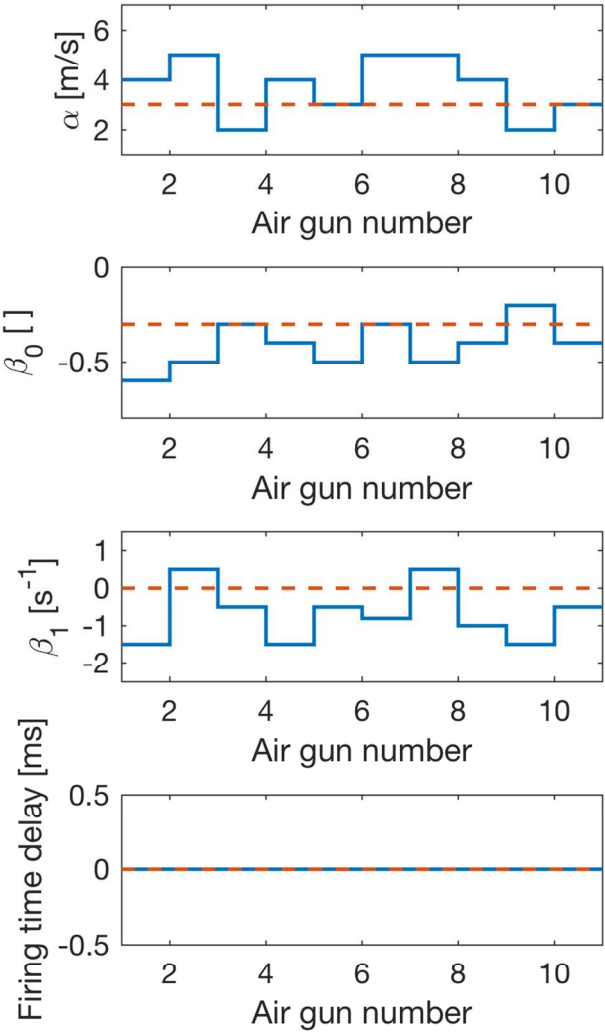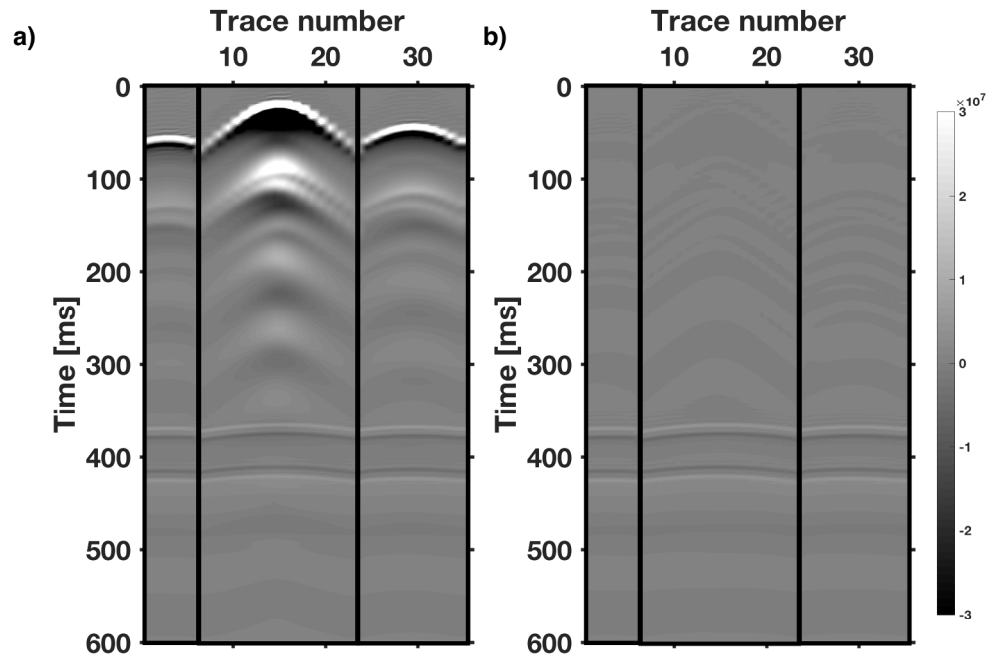
84x101mm (300 x 300 DPI)

1
2
3
4
5
6
7
8
9
10
11
12
13
14
15
16
17
18
19
20
21
22
23
24
25
26
27
28
29
30
31
32
33
34
35
36
37
38
39
40
41

Figure 3: Real (solid blue) and initial (dashed red) model parameters for synthetic inversion experiments.

84x152mm (300 x 300 DPI)

42
43
44
45
46
47
48
49
50
51
52
53
54
55
56
57
58
59
60

1
2
3
4
5
6
7
8
9
10
11
12
13
14
15
16
17
18
19
20
21
22
23
24
25
26
27
28
29
30
31
32
33
34
35
36
37
38
39
40
41
42
43
44
45
46
47
48
49
50
51
52
53
54
55
56
57
58
59
60

Figure 4: a) Modeled data from "real" model parameters, divided into three boxes corresponding to the three streamers. The distance between the traces is 12.5 m and the color bar represents amplitude. b) Difference between "real" data and modeled data after inversion. The subsurface reflections are not modeled by the inversion algorithm.

211x152mm (300 x 300 DPI)
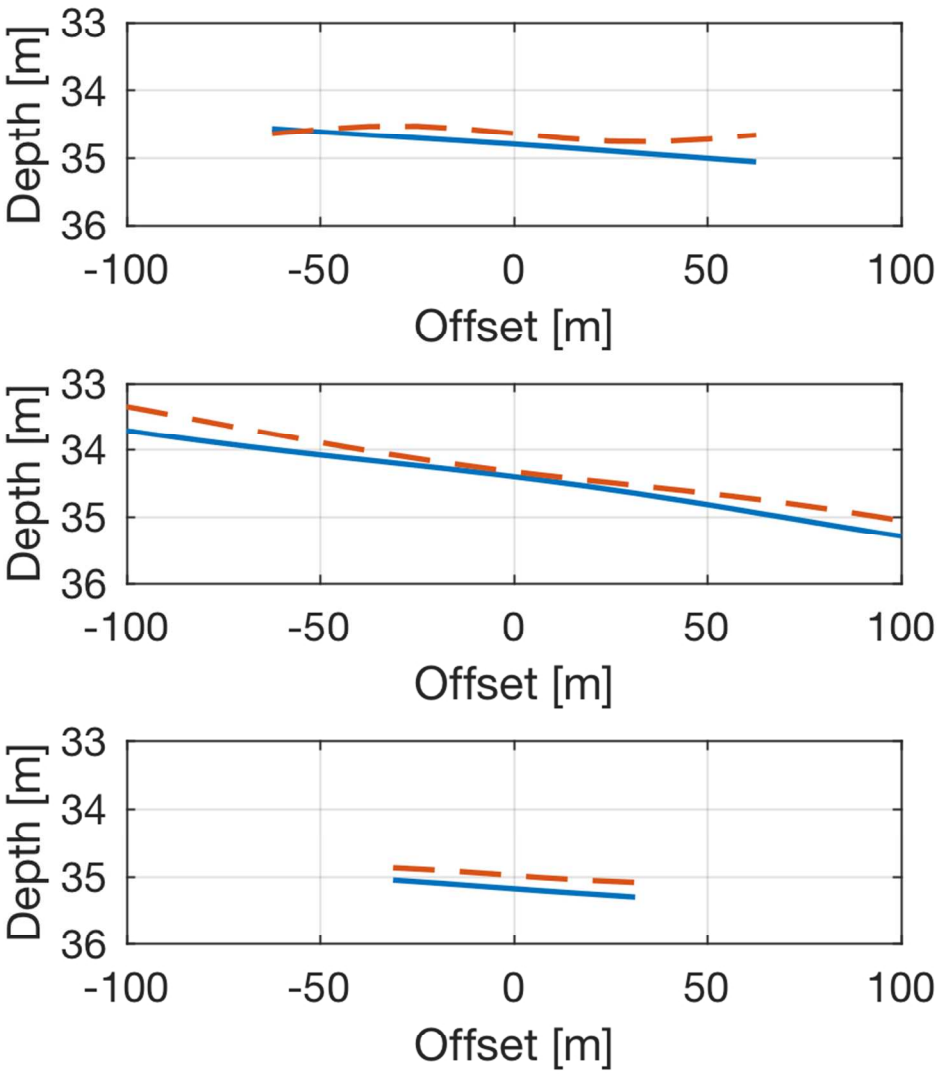
Figure 5: Real (solid blue) and estimated (dashed red) model parameters for the inversion.

84x101mm (300 x 300 DPI)
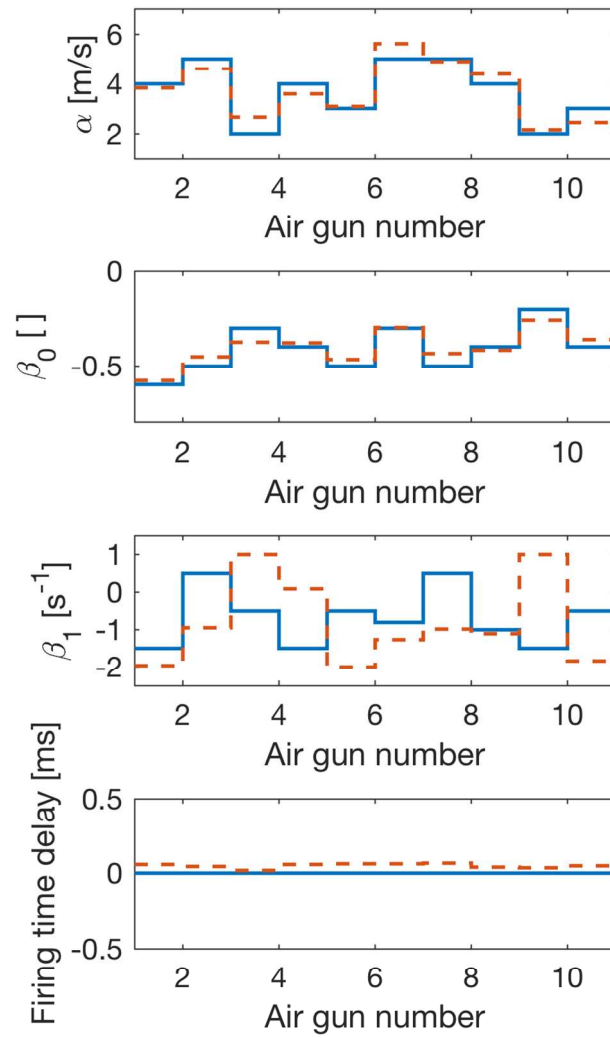
Figure 6: Real (solid blue) and estimated (dashed red) model parameters after the inversion.
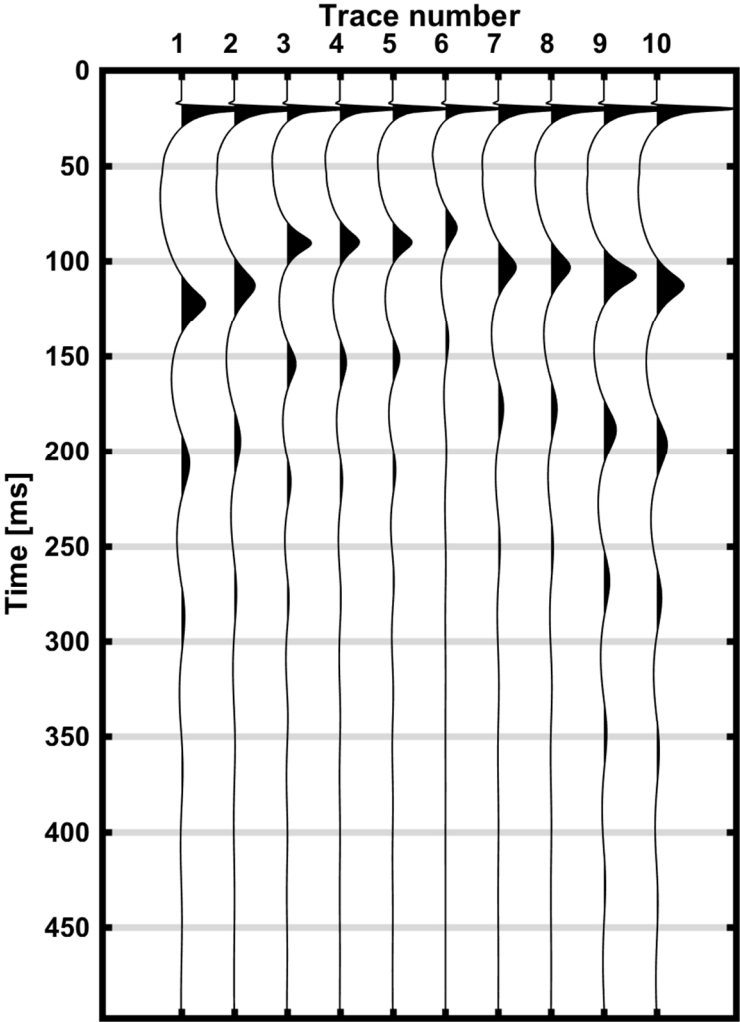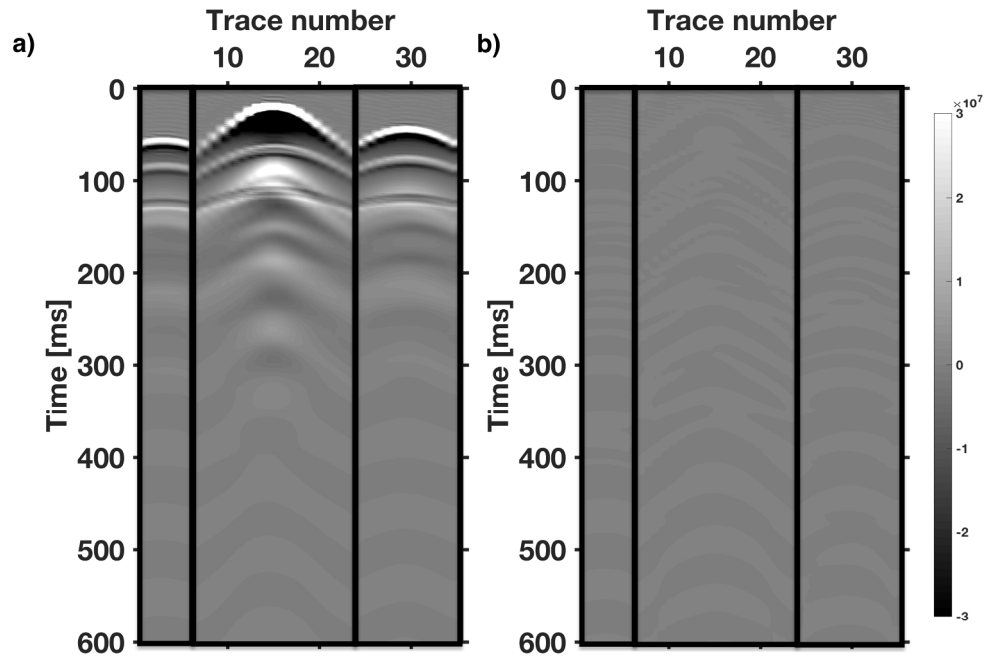
84x152mm (300 x 300 DPI)

1
2
3
4
5
6
7
8
9
10
11
12
13
14
15
16
17
18
19
20
21
22
23
24
25
26
27
28
29
30
31
32
33
34
35
36
37
38
39
40
41
42
43
44
45
46
47
48
49
50
51
52
53
54
55
56
57
58
59
60

Figure 7: Calculated notional source signatures from estimated model parameters after the inversion.

84x127mm (300 x 300 DPI)

Figure 8: a) Modeled data from "real" model parameters, divided into three boxes corresponding to the three streamers. The distance between the traces is 12.5 m and the color bar represents amplitude. b) Difference between "real" data and modeled data after inversion. The subsurface reflections are modeled by the inversion algorithm.
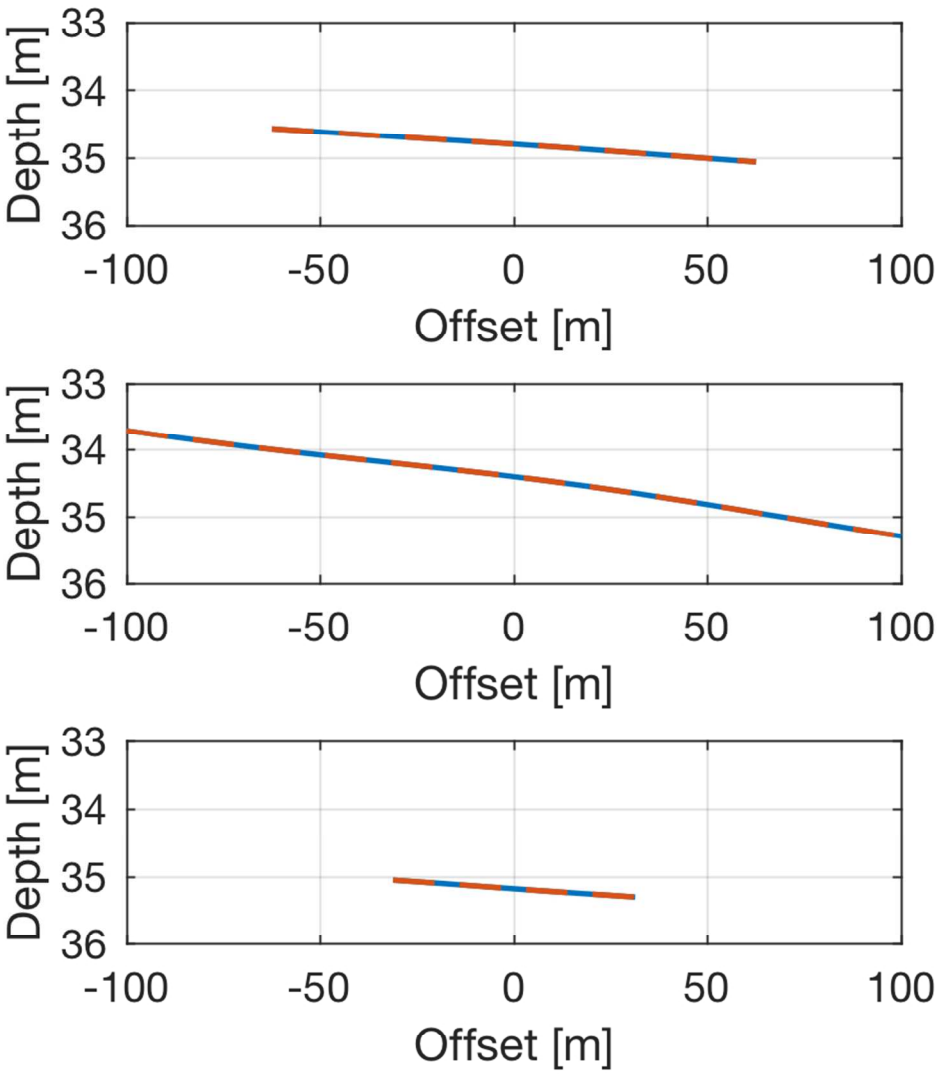
211x152mm (300 x 300 DPI)

1
2
3
4
5
6
7
8
9
10
11
12
13
14
15
16
17
18
19
20
21
22
23
24
25
26
27
28
29
30
31
32
33
34
35
36
37
38
39
40
41
42
43
44
45
46
47
48
49
50
51
52
53
54
55
56
57
58
59
60

Figure 9: Real (solid blue) and estimated (dashed red) streamer depths after the inversion.
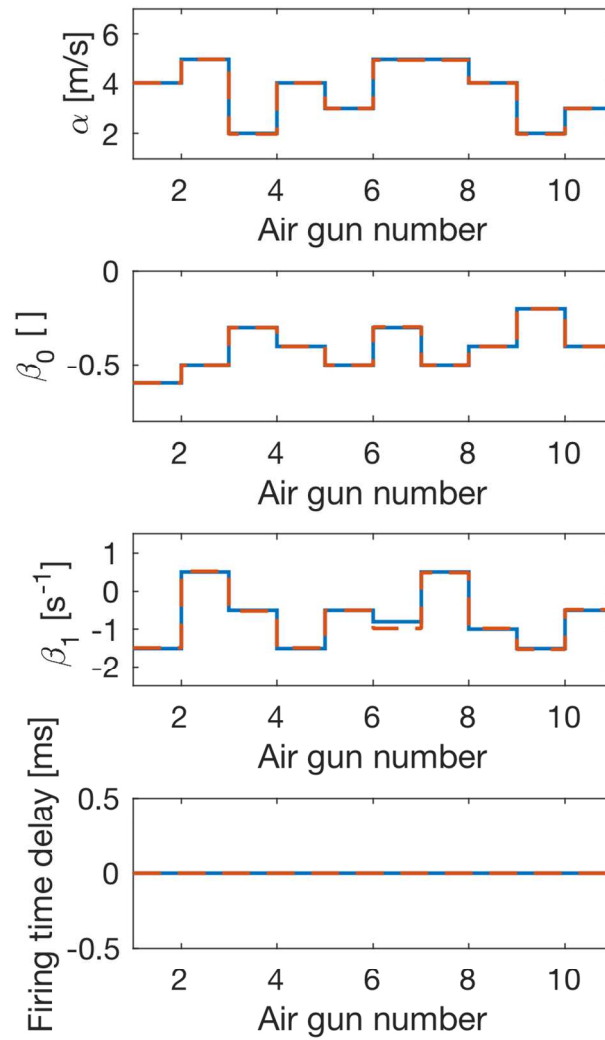
84x101mm (300 x 300 DPI)

Figure 10: Real (solid blue) and estimated (dashed red) model parameters after the inversion.
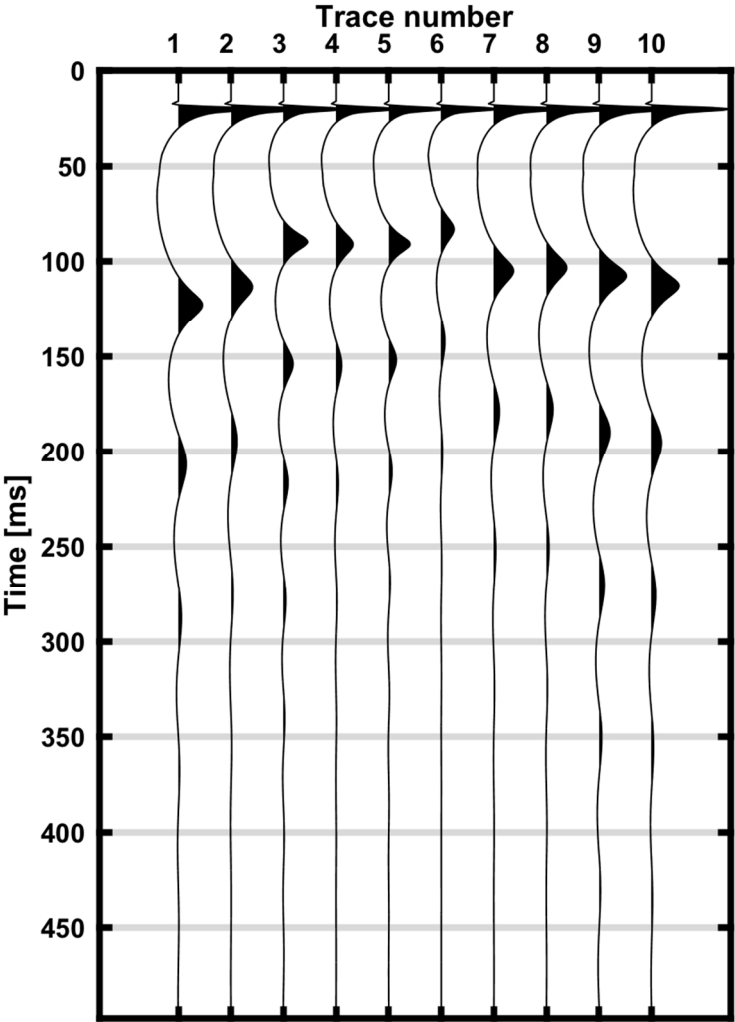
84x152mm (300 x 300 DPI)

Figure 11: Calculated notional source signatures from estimated model parameters after the inversion.
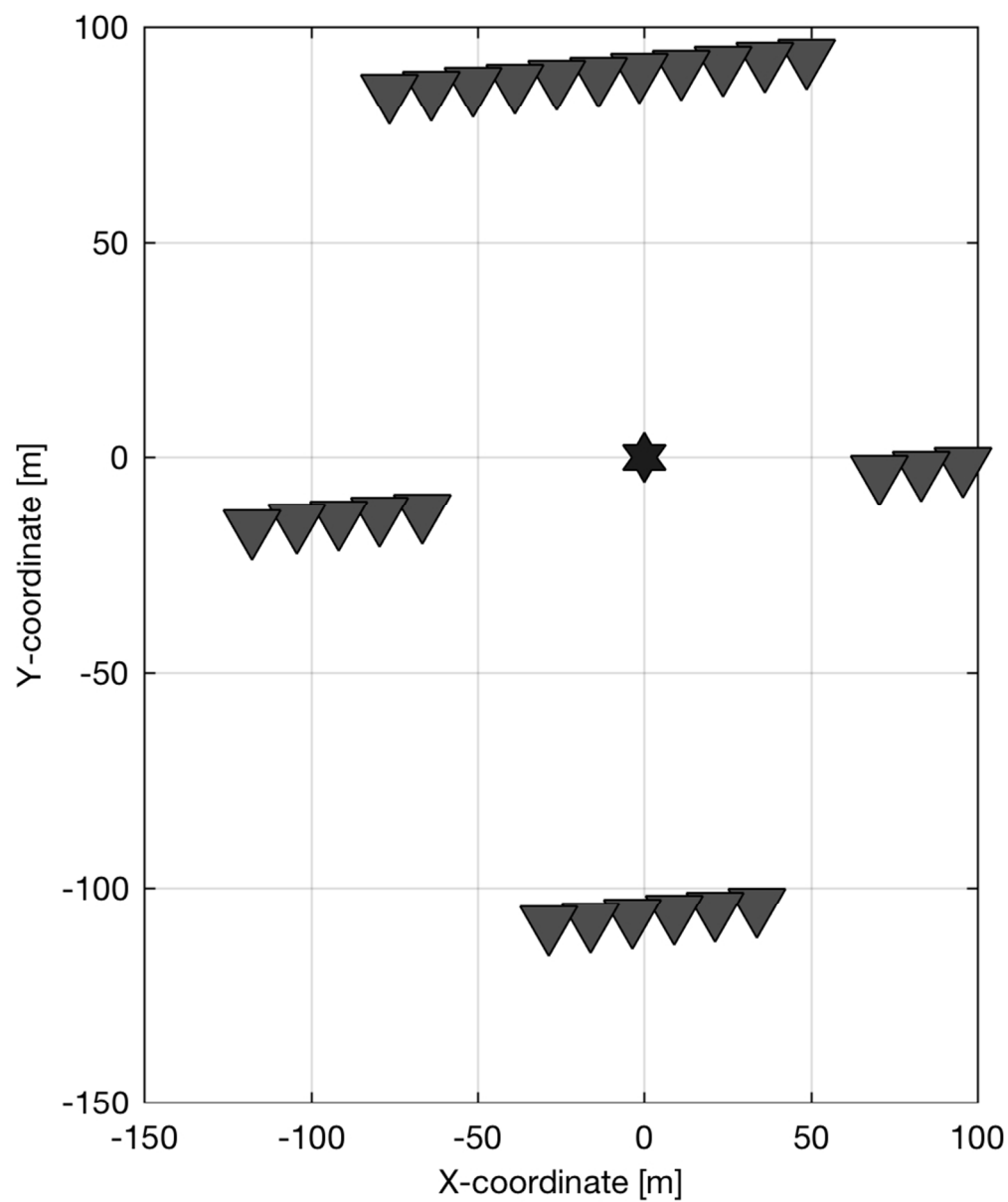
84x127mm (300 x 300 DPI)

Figure 12: Source center (star) and receiver (triangles) locations for the field data example.
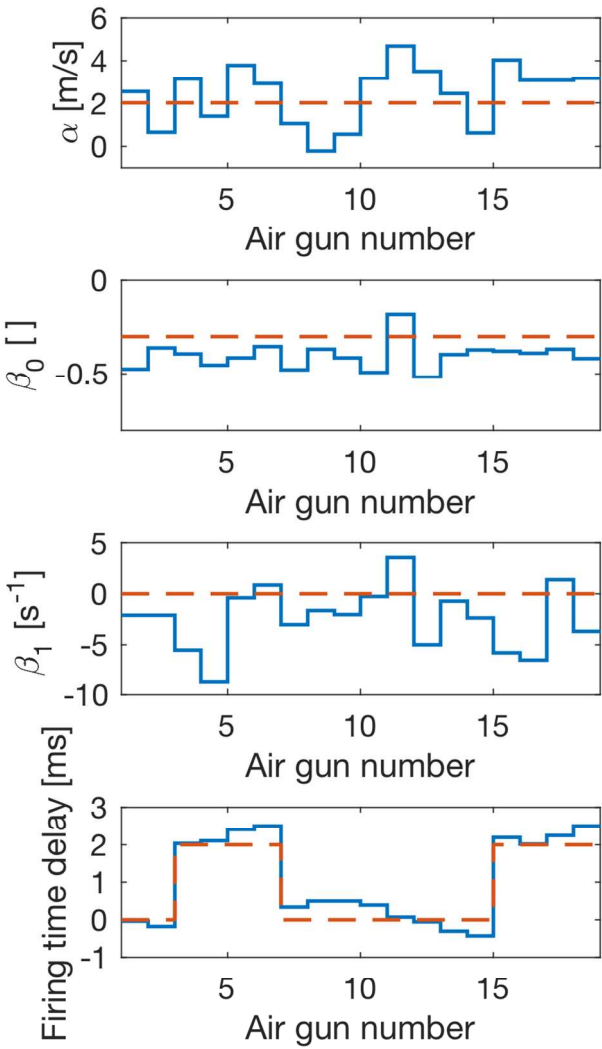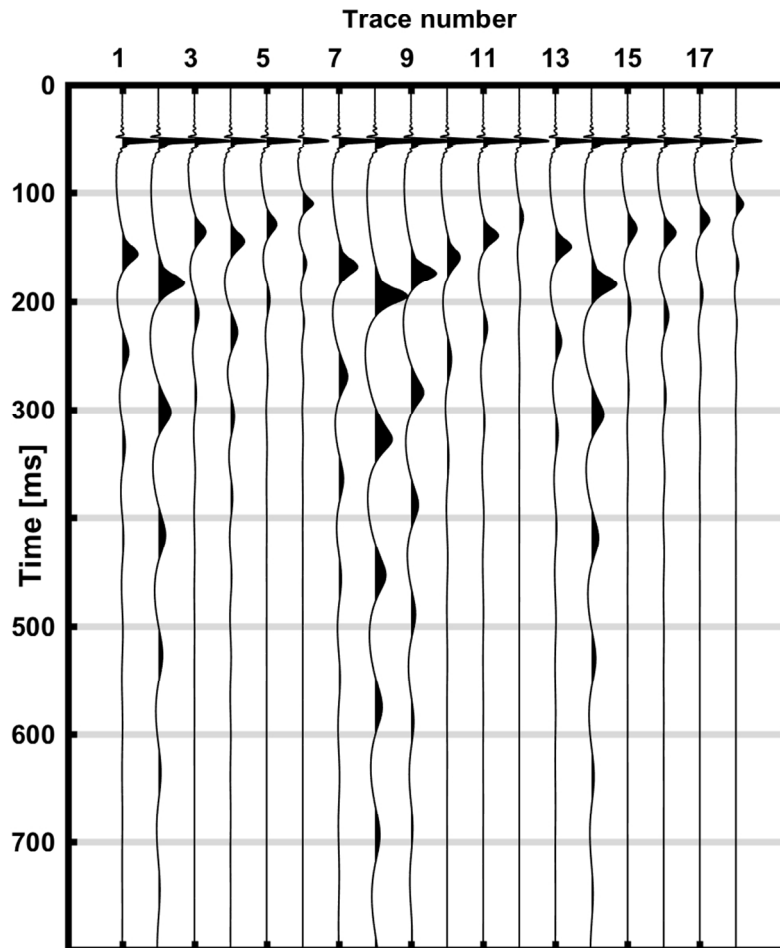
84x101mm (300 x 300 DPI)

1
2
3
4
5
6
7
8
9
10
11
12
13
14
15
16
17
18
19
20
21
22
23
24
25
26
27
28
29
30
31
32
33
34
35
36
37
38
39
40
41
42
43
44
45
46
47
48
49
50
51
52
53
54
55
56
57
58
59
60

Figure 13: Estimated (solid blue) and initial (dashed red) model parameters for field data example.‼ ┼

84x152mm (300 x 300 DPI)

Figure 14: Calculated notional source signatures from estimated model parameters after the inversion.

84x127mm (300 x 300 DPI)

1
2
3
4
5
6
7
8
9
10
11
12
13
14
15
16
17
18
19
20
21
22
23
24
25
26
27
28
29
30
31
32
33
34
35
36
37
38
39
40
41
42
43
44
45
46
47
48
49
50
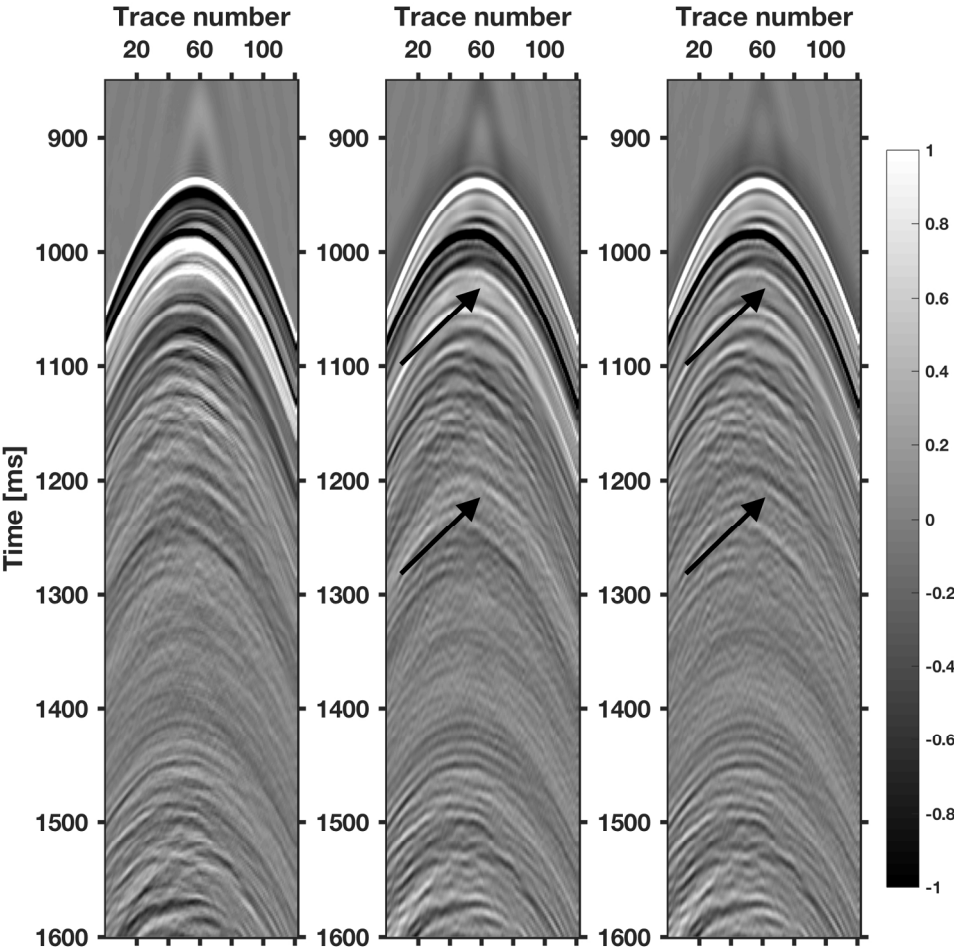51
52
53
54
55
56
57
58
59
60

Figure 15: Shot-gathers from field data example before source deghosting and designature (left) after source deghosting (middle) and after source deghosting and designature (right). The black arrows highlight low-frequency bubble energy in the deghosted shot-gather that appears to be zero-phased after designature.
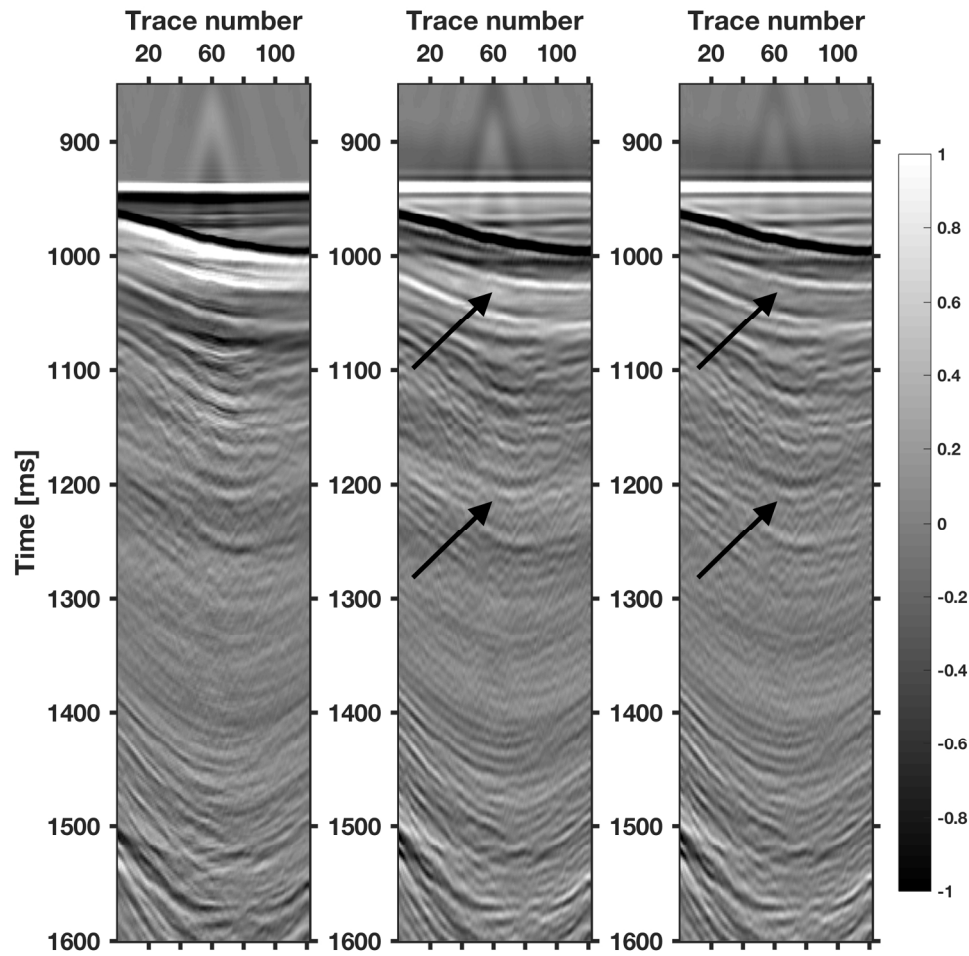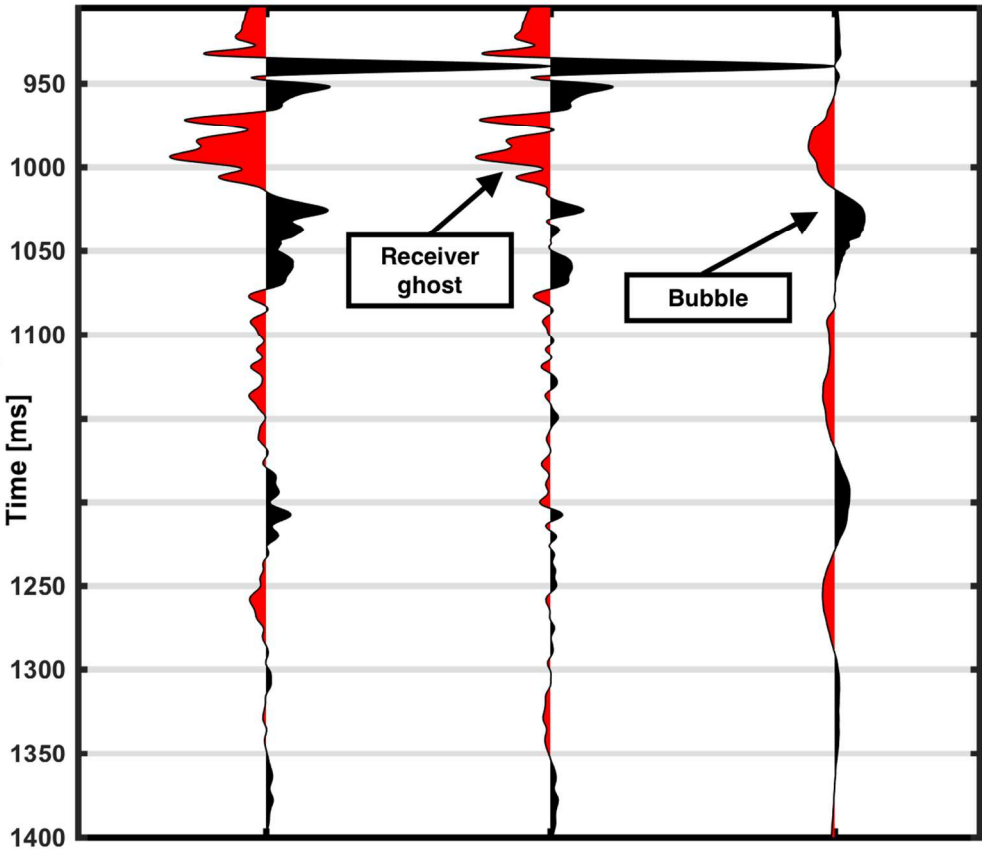
168x177mm (300 x 300 DPI)

Figure 16: Shot-gathers from Figure 15 after alignment of water bottom reflection: Input (left), after source deghosting (middle) and after source deghosting and designature (right). The black arrows highlight bubble energy in the deghosted shot-gather that appears to be zero-phased after designature. The receiver ghost does not align horizontally due to the variable-depth profile of the streamer.

168x177mm (300 x 300 DPI)

1
2
3
4
5
6
7
8
9
10
11
12
13
14
15
16
17
18
19
20
21
22
23
24
25
26
27
28
29
30
31
32
33
34
35
36
37
38
39
40
41
42
43
44
45
46
47
48
49
50
51
52
53
54
55
56
57
58
59
60

Caption : Figure 17: Left: Stack of deghosted shot-gather after alignment of water bottom reflection. Middle: Stack of deghosted and designatured shot-gather after alignment of water bottom reflection. Right: Difference.

110x127mm (300 x 300 DPI)